An integrated modeling and experimental approach to study hydrogen pickup mechanism in zirconium alloys

Authors: A. Couet[1*], L. Borrel[1], J. Liu[2], J. Hu[3], C. Grovenor[2]

[1]Department of Engineering Physics, University of Wisconsin-Madison, 1500 Engineering Drive, Madison, WI, 53703, United States
[2]Department of Materials, University of Oxford, Parks Road, OX1 3PH, United Kingdom
[3]Argonne National Laboratory, 9700 S. Cass Avenue, Argonne, IL, 60439, United States
*corresponding author: 425 Engineering Research Building, 1500 Engineering Drive, Madison, WI, 53703, United States; tel:+16082657955, email: couet@wisc.edu

1. Introduction and motivation

Hydrogen pick-up during the aqueous corrosion of nuclear fuel cladding is a critical life-limiting degradation mechanism in both Pressurized Water and Boiling Water Reactors. Indeed, hydrogen absorption can cause cladding embrittlement by hydride precipitation in the zirconium metal, resulting in severe reduction in service lifetime and hence the fuel burnup achieved [1] and technical challenges in the safe transportation and storage of spent nuclear fuel [2]. Hydrogen pickup is an integral part of the corrosion process because oxide growth and hydrogen pickup originate from a single electrochemical process [1, 3]. Although the development of modern commercial zirconium alloys has been aimed at reducing hydrogen pickup, the physical mechanisms controlling hydrogen transport and absorption are still unknown. It is, however, clear that alloying element additions, even at very low levels (below 1at%), have a significant impact on both the oxidation kinetics and the hydrogen pickup fraction, f_H, defined as:

$$f_H = \frac{\Delta_0^t H_{absorbed}}{\Delta_0^t H_{generated}} \quad (1)$$

where $\Delta_0^t H_{absorbed}$ is the hydrogen absorbed from the beginning of the corrosion test and $\Delta_0^t H_{generated}$ is the total amount of hydrogen generated by the corrosion reaction [4]. The experimentally measured hydrogen pickup fraction can be as low as 5% for Zr-0.5Nb alloys (in wt%) [5] to 30% for LK3 (an optimized version of Zircaloy-2) and even higher than 50% for Zircaloy-2 [6]. The low f_H values induced by Nb alloying additions have been the main driver for the development of industrial fuel cladding alloys such as ZIRLO™ and M5®. It is also well established that f_H is not constant, but varies significantly as function of corrosion time such that a single sample will show different total (and instantaneous) hydrogen pickup fractions

at different oxide thicknesses [4, 7]. However, it is still unclear if hydrogen absorption occurs through simple Fickian diffusion of neutral hydrogen across the oxide film or if charged hydrogen species (i.e. protons, hydroxide ions) are the vectors for hydrogen uptake. Oxide growth under cathodic or anodic polarization gives some evidence that the latter species is more prominent [8]. A physically based zirconium corrosion model which can correctly predict both the oxidation kinetics and hydrogen pickup behavior for zirconium alloys with different initial compositions and microstructures would be very valuable, but despite half a century of extensive research no such model has yet been developed.

Our starting point to investigate and model zirconium alloy corrosion is to focus on the effect of alloying elements. It is commonly observed that Zr-Nb alloys follow parabolic oxidation kinetics [9, 10] and have lower hydrogen pickup fractions than zirconium alloys containing Sn and transition metal elements (Fe, Cr, Ni) which show sub-parabolic kinetics and higher hydrogen pickup fractions [4, 11]. Consequently, current LWR's fuel claddings include approximately 1wt% of niobium to limit hydrogen pickup and thus hydride induced embrittlement [12]. In addition, Nb rich precipitates, either originally present in the cladding or induced by neutron irradiation, increase the cladding creep resistance [13]. As part of the work of the Mechanistic Understanding of Zirconium Corrosion (MUZIC) consortium [5, 14], a range of Zr-Nb alloys have been processed by Westinghouse and corroded in high pressure, high temperature pure water conditions (360 °C, 18 MPa) in a stainless steel autoclave for up to 300 days. From these, we have selected two alloys that showed parabolic corrosion kinetics but different initial microstructures (see Table 1).

Table 1 Detailed information on the samples used in this study

Alloys	Composition from combustion analysis(wt%)	Final annealing conditions
RXA Zr-0.5Nb tube	Zr-0.53Nb-0.04Fe	Recrystallized
Annealed Zr-1Nb sheet	Zr-0.91Nb-0.08Fe	Recrystallized then annealed at 720°C for 24hrs

The first alloy is Zr-0.5Nb with a final annealing step at 560 °C which leads to recrystallized α-Zr grains with the Nb mostly in solid solution and small Nb-containing second phase particles (SPPs). These SPPs are homogeneously distributed inside the grains, Figure 1 (a), and are mostly β-Nb with a few Zr-Nb-Fe phase particles. The Nb solid solution concentration has been determined by Atom Probe Tomography (APT) to be approximately

0.3 at% [15]. The second alloy is Zr-1.0Nb with a final annealing step of 24 hours at 720 °C. This is above the monotectoid temperature so that the microstructure is composed of recrystallized α-Zr grains with large Nb stabilized β-Zr (∼20% Nb) precipitates mostly at the α-Zr grain boundaries, Figure 1 (b), and a few smaller niobium-rich SPPs in the grain interiors. This initial microstructure is in good agreement with previous work on the β-Zr second phase distribution in high temperature annealed alloys [10]. Some phase separation of these larger metastable SPPs occurs after long term exposure at typical reactor temperatures [16], but APT analysis has shown that the solid solution concentration of Nb is still only 0.4 at% [17].

Samples were extracted from the autoclave at regular intervals to measure the average oxide thickness by weight gain measurements and the hydrogen concentrations by Vacuum Hot Extraction using a LECO® RHEN602, as detailed in [18]. The oxidation kinetics (a) and hydrogen pickup (b) are displayed in Figure 2 for both alloys. Although the alloying additions only differ by 0.5 wt% Nb, and the solid solution concentrations of Nb are rather similar, the oxidation kinetics are significantly different, with a faster corrosion rate for the Zr-1.0Nb (720 °C) alloy compared to the Zr-0.5Nb alloy (see Figure 2a). During testing up to 260 days, both alloys show the characteristic acceleration of oxidation kinetics (transition) at a similar oxide thickness between 3.1µm and 3.5µm, but this transition was considerably delayed in Zr-0.5Nb because of its slower corrosion rate.

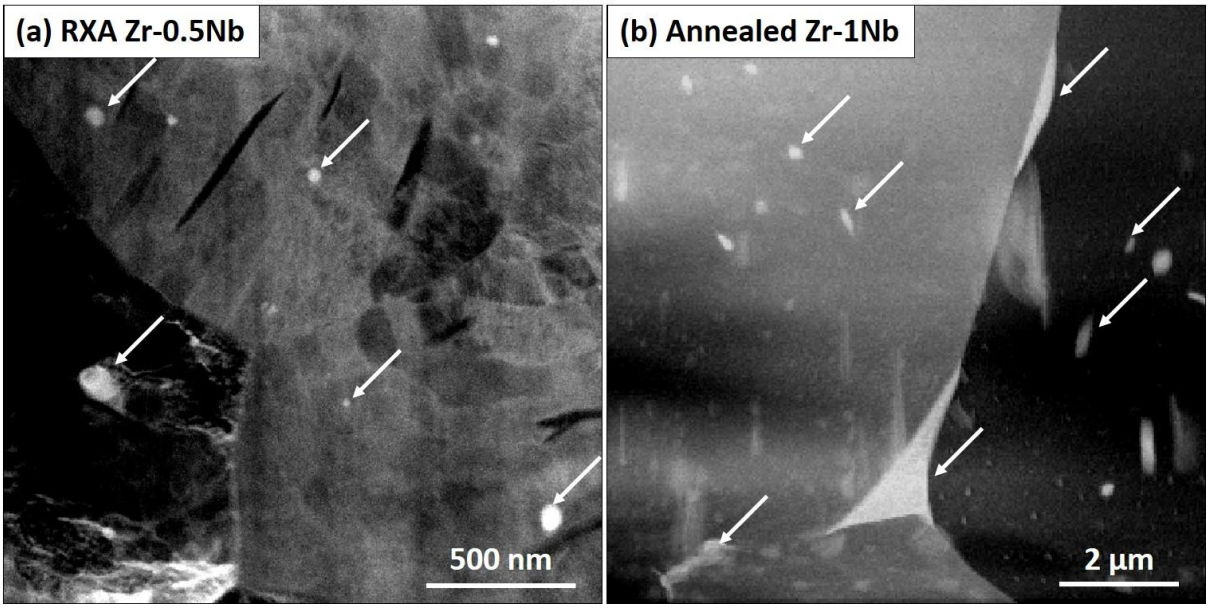

Figure 1: Typical microstructures of (a) Zr-0.5Nb and (b) Zr-1.0Nb (720°C) in STEM HAADF mode showing the different characteristic precipitate shapes and distribution.

As noted above, both alloys show parabolic oxidation kinetics as indicated by the power law fits:

$$\delta(t) = kt^n \quad (2)$$

with δ the oxide thickness and t the exposure time [19]. Even though the data in Figure 2 shows that the Zr-1.0Nb (720 °C) alloy goes into transition much earlier and displays overall a higher corrosion rate, the regular accelerations in oxidation rate simply follow the pre-transition oxide kinetics as shown by the power law fits. Thus the *pre-transition* oxidation kinetics that lead to an early onset of transition is mainly responsible for the higher corrosion rate of the Zr-1.0Nb (720 °C) alloy at long exposure times.

As detailed in [20, 21], parabolic oxidation kinetics is an indication of oxide local electro-neutrality, i.e. no bulk space-charge is generated across the oxide. Oxide electro-neutrality generally results in relatively larger corrosion rates [22]. While this condition is not necessarily observed in the oxidation of all zirconium alloys, oxide electro-neutrality has been verified in Zr-Nb alloys with enough Nb in solid solution in the oxide to compensate for the positive bulk space charge induced by the local difference in the concentration of diffusing species (such as oxygen vacancies, electrons and protons) [23], and these two alloys fall into that category as detailed in [20]. Consequently, it is expected that their oxidation mechanisms should be identical despite the higher oxidation rate of the Zr-1.0Nb

(720 °C) alloy, which may be due to the rather rapid dissolution of Nb from the β-Zr particles once embedded in the oxide while the β-Nb SPPs are known to experience delayed oxidation, preventing Nb from dissolving into the oxide [23].

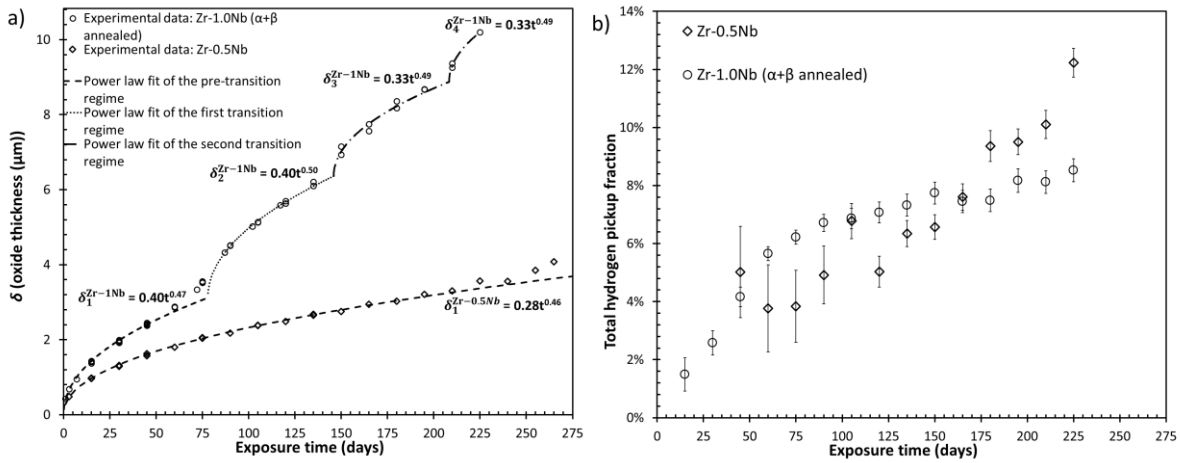

Figure 2: (a) Oxidation kinetics with experimental power law fits for the Zr-0.5Nb and annealed Zr-1.0Nb materials. (b) Total hydrogen pickup fractions as function of exposure time for both alloys. The corrosion conditions are described in [5].

Both alloys, as expected, show lower hydrogen pickup fractions than typically reported for Zircaloys because of the beneficial effect of Nb additions [4, 9]. The hydrogen pickup fraction trends are also similar in both alloys, with an increase in f_H before transition (i.e. while the oxide is still protective), and not *at* transition [4, 7] since very similar values of f_H are measured on either side of the transition point. It is worth noting that although the oxidation kinetics are quite faster for Zr-1.0Nb (720 °C) alloy compared to Zr-0.5Nb, the total hydrogen pickup fractions are quite similar with the Zr-1.0Nb (720 °C) alloy reaching a plateau around 8%, while the Zr-0.5Nb picks up at around 10% before transition.

As stated above, no corrosion models have been developed to correctly predict both hydrogen pickup and oxidation kinetics simultaneously. This study aims at filling this gap by combining recently developed physically based corrosion models with new observations from careful characterization of the nanostructure of the oxide scales.

2. Modelling using the Coupled Current Charge Compensation (C4) corrosion model

2.1. Review of the C4 model and implementation of hydrogen pickup

The framework of the C4 model has been extensively derived in [20] and only a brief description will be given here. The overall objectives of the model are (i) to provide an explanation for the observed value of the exponent n in equation (2) and (ii) to rationalize measured differences in oxidation kinetics and hydrogen pickup fractions between alloys based on their compositions. The model arrives at the oxidation kinetics and hydrogen pickup fraction by solving mobility equations for the atomic species migrating in the oxide layer under electro-chemical potential driving forces, with the imposition of a coupled-current condition of net zero charge transport through the film at all times:

$$\sum_{s}^{\substack{diffusing\\species}} Z_s \vec{J}_s = 2\,\mathrm{J}_{V_{\ddot{O}}} - \mathrm{J}_{\mathrm{e}'} - \mathrm{J}_{H^{\cdot}} = 0 \tag{3}$$

It is emphasized that this condition is less restrictive and more physical than the overall electro-neutrality equation often adopted in other corrosion models [24, 25]. The Poisson equation can be explicitly solved [26], but in the particular case of the Nb alloys studied here it has been shown using synchrotron micro X-Ray Absorption Near-Edge Spectroscopy (XANES) that there is enough Nb in solid solution in the oxide to, at first order, compensate for the concentration differences of the diffusing species, namely oxygen vacancies, $\mathrm{V}_{\ddot{\mathrm{O}}}$, interstitial protons, $H^{\cdot}$, and electrons, e' [20, 23, 27]. Thus the following condition is satisfied everywhere in the oxide:

$$E_{sp}(x) = \frac{4\pi e}{\varepsilon\varepsilon_0}\int_0^x \left(2C_{\mathrm{V}_{\ddot{\mathrm{O}}}}(l) + C_{H^{\cdot}}(l) - C_{\mathrm{e}'}(l) - (4-m)C_{\mathrm{Nb}^{(4-\mathrm{m})\prime}}(l)\right)\mathrm{d}l \ll E_0 \tag{4}$$

where E_{sp} is the space charge induced electric field in the bulk oxide, x the position in the oxide ($x = 0$ being the oxide-metal interface), e the Coulomb charge, ε the relative permittivity of ZrO_2, ε_0 the vacuum permittivity in F·m^{-1}, $C_s(l)$ the concentration of the species s at the at oxide position l, with s being $\mathrm{V}_{\ddot{\mathrm{O}}}$, $H^{\cdot}$, e' or substitutional Nb cations with oxidation state m, $\mathrm{Nb}^{(4-\mathrm{m})\prime}$, and E_0 is the homogenous electric field as defined in [21]. As described in [20], if equation (4) is satisfied, then the oxidation kinetics are indeed parabolic ($n = 0.5$), as they are for the two Zr-Nb alloys studied in this paper, Figure 2(a). On the other hand if the space charge induced electric field is not negligible compared to the homogeneous electric field, the oxidation kinetics are sub-parabolic ($n < 0.5$). It is remarkable that there is an analytical solution for this system of equations. Following a

similar derivation to that in [20], but with the addition of the proton current, the oxide thickness δ (in micrometers) and the hydrogen content in the metal $C_{\mathrm{Zr}}^{\mathrm{H}}$ (in wt·ppm) at a given exposure time t are given by the following equations:

$$\delta(t) = \sqrt{V_m \gamma_{\mathrm{V_O^{\cdot\cdot}}} t} \tag{5}$$

where V_m is the zirconium oxide molecular volume equal to $3.6 \times 10^{-23}\mathrm{cm}^3/\mathrm{molecule}$, and $\gamma_{\mathrm{V_O^{\cdot\cdot}}}$ is a constant given by:

$$\gamma_{\mathrm{V_O^{\cdot\cdot}}} = \mu_{\mathrm{V_O^{\cdot\cdot}}}\, k_{\mathrm{B}}\, T \ln(\eta) \cdot \left(\frac{C_{\mathrm{o/w}}^{\mathrm{V_O^{\cdot\cdot}}} - C_{\mathrm{o/m}}^{\mathrm{V_O^{\cdot\cdot}}}\, \eta^2}{1 - \eta^2} \right) \text{ with } \eta = e^{\delta \frac{eE_0}{k_{\mathrm{B}} T}} \tag{6}$$

where k_{B} is the Boltzmann constant, T the temperature in Kelvin, $C_{\mathrm{o/m}}^{\mathrm{V_O^{\cdot\cdot}}}$ the oxygen vacancy concentration at the oxide/metal interface in vacancies·cm^{-3}, $C_{\mathrm{o/w}}^{\mathrm{V_O^{\cdot\cdot}}}$ the oxygen vacancy concentration at the oxide/water interface in vacancies·cm^{-3} and $\mu_{\mathrm{V_O^{\cdot\cdot}}}$ is the oxygen vacancy mobility defined in [20] as:

$$\mu_s = \frac{4\, a^2 \nu\, Z_{\mathrm{s}}}{k_{\mathrm{B}}\, T} e^{-\frac{E_{\mathrm{m}}^{\mathrm{S}}}{k_{\mathrm{B}} T}} \tag{7}$$

where a is the migration jump distance in the oxide (cm), ν the migration jump frequency in s^{-1}, Z_s the charge of the s species and E_{m}^{S} the migration energy of the s species (in eV). The constant η is the solution of the second order equation $\mathrm{A}\,\eta^2 + \mathrm{B}\,\eta + \mathrm{D} = 0$ derived from the coupled current equation (3) with:

$$\begin{aligned} \mathrm{A} &= \mu_{\mathrm{e'}}\, C_{\mathrm{o/w}}^{\mathrm{e'}} - 2\,\mu_{\mathrm{V_O^{\cdot\cdot}}}\, C_{\mathrm{o/m}}^{\mathrm{V_O^{\cdot\cdot}}} - \mu_{\mathrm{H^{\cdot}}}\, C_{\mathrm{o/m}}^{\mathrm{H^{\cdot}}}, \\ B &= \mu_{\mathrm{e'}}\, (C_{\mathrm{o/w}}^{\mathrm{e'}} - C_{\mathrm{o/m}}^{\mathrm{e'}}) + \mu_{\mathrm{H^{\cdot}}} \left(C_{\mathrm{o/w}}^{\mathrm{H^{\cdot}}} - C_{\mathrm{o/m}}^{\mathrm{H^{\cdot}}} \right), \\ D &= 2\,\mu_{\mathrm{V_O^{\cdot\cdot}}}\, C_{\mathrm{o/w}}^{\mathrm{V_O^{\cdot\cdot}}} - \mu_{\mathrm{e'}}\, C_{\mathrm{o/m}}^{\mathrm{e'}} + \mu_{\mathrm{H^{\cdot}}}\, C_{\mathrm{o/w}}^{\mathrm{H^{\cdot}}} \end{aligned} \tag{8}$$

where the mobility μ_{s} and interfacial concentrations $C_{\mathrm{o/w}}^{\mathrm{s}}$ and $C_{\mathrm{o/m}}^{\mathrm{s}}$ are defined for each species s.

On the other hand, the hydrogen concentration in the metal, $C_{\mathrm{Zr}}^{\mathrm{H}}$, is defined by:

$$C_{\mathrm{Zr}}^{\mathrm{H}}(t) = \frac{C_{\mathrm{Zr}}^{\mathrm{H}}(0) \cdot\ m_{\mathrm{Zr}}(0) + \mathrm{wg}_{\mathrm{H}}(t)\ \cdot \mathcal{A}}{m_{\mathrm{Zr}}(t)} \tag{9}$$

where wg_{H} is the hydrogen weight gain in mg·dm^{-2}, $\mathcal{A}$ the area of the sample and $m_{\mathrm{Zr}}(t)$ its mass. It is assumed that the hydrogen concentration in the metal $C_{\mathrm{Zr}}^{\mathrm{H}}(t)$ is equal to the hydrogen concentration at the oxide/metal interface, $C_{\mathrm{o/w}}^{\mathrm{H}\cdot}(t)$, times the ratio of the metal and oxide densities. We believe that this assumption is reasonable since the hydrogen diffusivity in zirconium is relatively high [12].

The hydrogen weight gain is given by:

$$\mathrm{wg}_{\mathrm{H}}(t) = J_{\mathrm{H}\cdot}(t) \cdot \frac{M_{\mathrm{H}}}{\mathcal{N}_A} \cdot t \tag{10}$$

where M_{H} is the molar mass of hydrogen in g·mol^{-1}, $\mathcal{N}_A$ is Avogadro's number and $J_{\mathrm{H}\cdot}(t)$ the flux of hydrogen at the oxide/metal interface in hydrogen·cm^{-2}·s^{-1} defined by:

$$J_{\mathrm{H}\cdot} = \mu_{\mathrm{H}\cdot}\ k_{\mathrm{B}}\ T \ln(\eta) \cdot \left(\frac{C_{\mathrm{o/m}}^{\mathrm{H}\cdot}\ \eta -\ C_{\mathrm{o/w}}^{\mathrm{H}\cdot}}{1-\eta} \right) \tag{11}$$

where the definitions are the same as in (6) but for protons. It is emphasized that this is the first time that an analytical solution has been derived for the transport of three charged species across a growing oxide, and this is critical for the optimization of parameters as detailed below. The algorithm to solve this set of equations is outlined in the supplementary material attached to this study.

2.2. C4 model parameters

Although the number of parameters is limited (i.e. the three migration energies and the interfacial concentrations), it is essential to determine which ones must be used as fitting parameters of *both* the oxidation and hydriding kinetics and which ones can be confidently determined from physical considerations and the literature.

As detailed extensively in [20, 28], the concentrations of electrons and vacancies at the oxide/water interface are essentially zero since the interfacial reaction kinetics are very rapid in comparison to charged species transport across the oxide. The exact value of the sub-stoichiometry of the ZrO_2 phase at the oxide/metal interface is a subject of significant

controversy in the scientific community. Indeed, although this sub-stoichiometry has to be present to induce thermal oxide growth, it has never been detected experimentally, even by atomic scale analytical techniques such as Atom Probe Tomography (APT) [29]. Thus, the zirconium oxide sub-stoichiometry domain has to be extremely limited. As detailed in [20], a sub-stoichiometry of 0.75% ($ZrO_{1.985}$), corresponding to an oxygen content of 66.16 at% compared to the stoichiometric 66.67 at%, is chosen in accordance with [30]. That corresponds to an oxygen vacancy concentration at the oxide/metal interface $C_{\mathrm{o/m}}^{\mathrm{V_O^{\cdot\cdot}}}$ equal to $4.2 \times 10^{20}\ \mathrm{vacancies} \cdot \mathrm{cm}^{-3}$. Although this concentration is already very small, it is recognized that the level of sub-stoichiometry could be even lower than this, as suggested by the ab-initio modelling results in [31, 32]. This implies that the electric field across the oxide plays a significant role in controlling the diffusion of charged species compared to the chemical potential driving force, as confirmed in [20, 33, 34].

The concentration of hydrogen at the oxide/metal interface $C_{\mathrm{o/m}}^{\mathrm{H^{\cdot}}}$ is supposed to be in equilibrium with that in the bulk metal because hydrogen diffusivity in Zr is extremely fast [35] such that combustion results as function of time shown in Figure 3 were chosen. The electron concentration at the oxide/metal interface is then chosen to compensate for the overall charge imbalance from vacancies and protons. Suboxides, such as ZrO and Zr(Osat), sometimes observed during post-corrosion TEM analysis, are not modeled in this study because of the limited reported data set as well as the lack of knowledge about the suboxide properties.

2.3. Modeling results and parametric optimization

The remaining unknown parameters are the three migration energies and the concentration of protons at the oxide/water interface, $C_{\mathrm{o/w}}^{\mathrm{H^{\cdot}}}$. Since the oxidation kinetics follow a parabolic law for the materials studied in this paper, we assume that the oxide scale remains dense and protective to oxygen diffusion up to the transition thickness at about 3.1 µm. Thus, the oxygen vacancy migration energy is chosen to be constant as a function of exposure time. Electron conduction in the oxide layer arises from thermal ionization of shallow donor states or centers into the conduction band followed by relaxation into empty energy states in the band gap [36, 37] rather than direct promotion from the valence to the

conduction band. Here it is assumed that the electron migration energy is also constant and the same in the oxide scales on both Zr-Nb alloys.

Using these assumptions, a careful optimization procedure has been performed to fit the oxidation *and* hydriding kinetics in both alloys using the fitting parameters detailed above. The optimization algorithm adjusts the value of the hydrogen migration energy at each time step in order to minimize the difference between the experimental data and the model prediction for hydrogen concentration in the cladding. The choice of hydrogen migration energy as a fitting parameter rather than the hydrogen concentration at the oxide/water interface is discussed at the end of this section. The results for both alloys are plotted in Figure 3.

Since the transition in oxide growth kinetics is not modeled in our approach because stresses are not taken into account [38, 39], a novel stochastic approach to transition has been developed. The details of this approach are included in the Appendix and the results shown in Figure 3(b). Both oxidation and hydriding kinetics are very well reproduced by the C4 model. The only empirical parameter in these results is the exposure time to transition, optimized based on the probabilistic approach detailed in the Appendix.

The migration energies for oxygen vacancies, electrons and protons as function of exposure time are plotted in Figure 4. As detailed above, constant values of oxygen vacancy migration energies and electron untrapping energy have been used to fit both oxidation and hydriding kinetics. The electron untrapping energy is identical in the two alloys since the hopping mechanism is assumed to occur via the same defect energy levels in the band gap, most likely those created by the oxygen vacancies themselves [40]. Although ab-initio calculations have reported that the electronic energy levels of oxygen vacancies are located approximately at 0.8 eV for $V_{\ddot{O}}$ and 1.2 eV for $V_{\dot{O}}$ below the zirconia conduction band [40, 41], a value of 1.35 eV gives the best fit for both Zr-Nb alloys in this study. On the other hand, the best fit oxygen vacancy migration energy is slightly smaller in the Zr-1.0Nb (720 °C) alloy (1.43 eV) compared to the value in Zr-0.5Nb (1.52 eV), potentially due to the effect of β-Zr on oxidation kinetics detailed in [10, 42, 43]. It is noted that these charged oxygen vacancy migration energy are higher than what has been reported in the literature by DFT

calculations [44-47]. However, the oxygen vacancy migration energy could be higher than the one reported by DFT for the following reasons:

- The oxide is under compressive in-plane stress due to the oxide volume expansion. This compressive stress would induce higher migration energies for the oxygen vacancy to diffuse through the oxide.
- A significant fraction of twin boundaries are present in the zirconium oxide [48]. According to the study in [49], the triple points, where twin boundaries meet grain boundaries, decrease the atomic oxygen transport rate by one order of magnitude. Considering that most vacancies diffuse through the grain boundaries during oxidation, if the twin boundaries are present in the oxide during corrosion, they could alter the diffusion of oxygen atoms by increasing the vacancy migration energy.

As mentioned above, the last relatively unknown parameter is the proton concentration at the oxide/metal interface, which depends on the material and comes from experimental data obtained using hot vacuum extraction [5]. The proton concentration at the oxide/water interface is chosen to be constant and equal to 880 wt·ppm for both alloys [50].

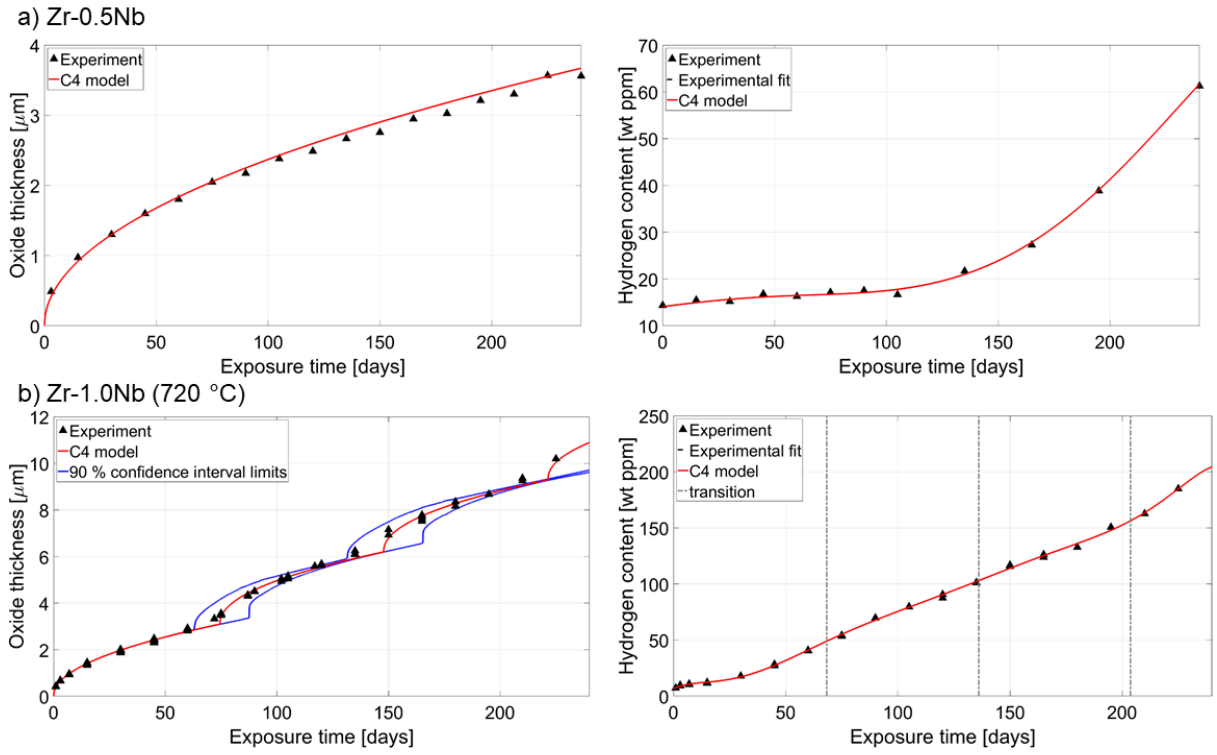

Figure 3: Oxide thickness (µm) and hydrogen content (wt·ppm) values as function of exposure time for (a) Zr-0.5Nb and (b) Zr-1.0Nb (720 °C) alloys. Triangles are experimental data while the red curves are the results from the C4 model

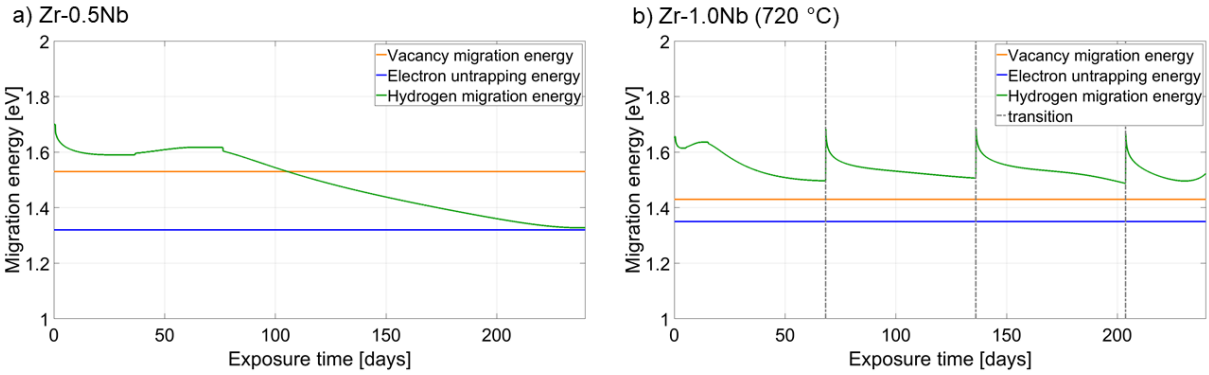

Figure 4: Migration energies for the three diffusing species as function of exposure time extracted from the C4 model for (a) Zr-0.5Nb and (b) Zr-1.0Nb (720 °C) alloys.

It is noted that, in Figure 4, the Zr-1.0Nb (720 °C) proton migration energies after transition are slightly higher than the initial migration energy. This observation is likely due to errors related to the discontinuity induced by the sudden transition in oxidation rate. On the other hand, the apparent increase in proton migration energy towards the end of the exposure time is due to the lack of experimental data points at this high exposure time Indeed, not enough data points are present in the fourth transition regime to correctly model the evolution of hydrogen content and weight gain with high accuracy. The results give a total hydrogen content in the oxide equal to 250 wt·ppm, which is of the same order of magnitude as literature results using fractionated vacuum hot extraction [50]. It is interesting to note that the hydrogen pickup is a natural outcome of the C4 model and that the homogeneous positive electric field is not preventing hydrogen absorption by the Zr metal. All the modelled parameters are summarized in Table 2

Table 2 Parameters used in this study for the two Zr-Nb alloys

	Alloy	
Parameters	Zr-0.5Nb	Zr-1.0Nb (annealed)
Vacancy migration energy (eV)	1.52	1.43
Proton migration energy (eV) at the start	1.65	
Electron untrapping energy (eV)	1.35	
Concentration of vacancies at the O/W interface ($C_{o/m}^{V_O^{\cdot\cdot}}$)	10^{17} vacancies·cm^{-3}	

Concentration of vacancies at the O/M interface ($C^{V_O^{\cdot\cdot}}_{o/w}$ (ZrO2-x))	66.16 at% ($ZrO_{1.985}$)
Concentration of protons at the O/W interface ($C^{H^{\cdot}}_{o/m}$ in wt·ppm)	880 wt·ppm
Concentration of protons at the O/M interface ($C^{H^{\cdot}}_{o/w}$ in wt·ppm)	From Figure 3

2.4. Implications of the outcomes of the C4 model

An important outcome of this study is that in order to correctly reproduce the measured oxidation and hydriding kinetics for both alloys the proton migration energy *has* to decrease as transition is approached. For both alloys, the initial proton migration energy is benchmarked at 1.65 eV and decreases steadily until transition. Since the transition occurs earlier for Zr-1.0Nb (720 °C), the proton migration energy decreases only to 1.5 eV at transition, while it decreases to 1.35 eV in the case of Zr-0.5Nb. For the Zr-1.0Nb (720 °C) alloy that shows multiple transitions. This is consistent with a higher total hydrogen pickup fraction for Zr-0.5Nb compared to Zr-1.0Nb (720 °C) observed in Figure 2b. This behavior is also reproduced almost identically from one transition to another, suggesting that hydrogen pickup follows the periodic corrosion kinetics very closely even though this periodicity in the hydriding kinetics is not easy to detect in the rather dilute experimental dataset in Figure 3. Consequently, the model leads to the proposition that as the oxide grows it becomes gradually more permeable to hydrogen diffusion but not to oxygen permeation since the oxide is still electrochemically protective before the transition thickness.

We discuss in the next section the microstructural features that could be responsible for the modelled decrease in proton migration energy through the oxide before transition. Before doing so, it is noted that the optimization algorithm used to modify the value of the hydrogen migration energy to fit the hydrogen concentration in the cladding can instead be used with the hydrogen concentration at the oxide/water interface as a fitting parameter. However, in that case, the result of this study shows that a hydrogen concentration of more than 10^5 wt·ppm is needed at the oxide/water interface to fit the hydrogen content in the cladding using literature values for the hydrogen diffusion coefficient in the oxide [51-53], which is at least one order of magnitude higher than what has been reported in the literature [50]. On the other hand, using the hydrogen migration energy as a fitting parameter bounds this parameter between 1.7eV and 1.3eV (see Figure 4), while the

hydrogen content at the oxide/water interface is set at 880 wt·ppm (see Table 2), which appears much more realistic [50].

3. Microstructure and microchemistry characterization of the oxide layers

In order to explore possible pathways for hydrogen permeation through the oxide layers on the two Zr alloys by transmission electron microscopy, we have selected the most appropriate imaging technique, Fresnel contrast, and used it for quantitative analysis of nanoscale porosity in oxides on the Zr-0.5Nb alloy well before (75 days) and close (165 days) to transition, and for a more qualitative study of porosity in the oxide grown on the Zr-1.0Nb (720 °C) alloy for 91 days and so lying between the first and second transitions in Figure 2 (b).

3.1. Experimental procedures

Cross-sectional transmission electron microscopy foils containing both the oxide layer and the metal matrix were prepared for the study of nano-porosity using the in-situ FIB lift-out method on a Zeiss Crossbeam 540 FIB/SEM system. Following the steps defined in [54], lamellar specimens were lifted out and welded to a 3mm Cu grid using an in-situ micro-manipulator. Progressive thinning with a gradually reducing milling current of 1500-100pA at 30kV was performed on both sides of the foil. Final thinning and cleaning was performed at 5kV and 200pA to electron transparency. TEM characterization of the type and distribution of porosity was carried out using a JEOL 2100 microscope operated at 200kV. Fresnel contrast in TEM imaging originates from the difference in the inner potential of the sample matrix and any buried pores, and depends on thickness variations along the direction of the incident electron beam [55]. This imaging mode can clearly reveal the morphology and distribution of nano pores as small as 1nm, and Figure 5 shows an example of how nano-porosity of different types can be detected in a typical fine grained polycrystalline zirconium oxide corrosion product layer on Zr-0.5Nb alloy imaged under Fresnel conditions. When the image is over-focused, buried pores show dark contrast and the same defects are bright when under-focused.

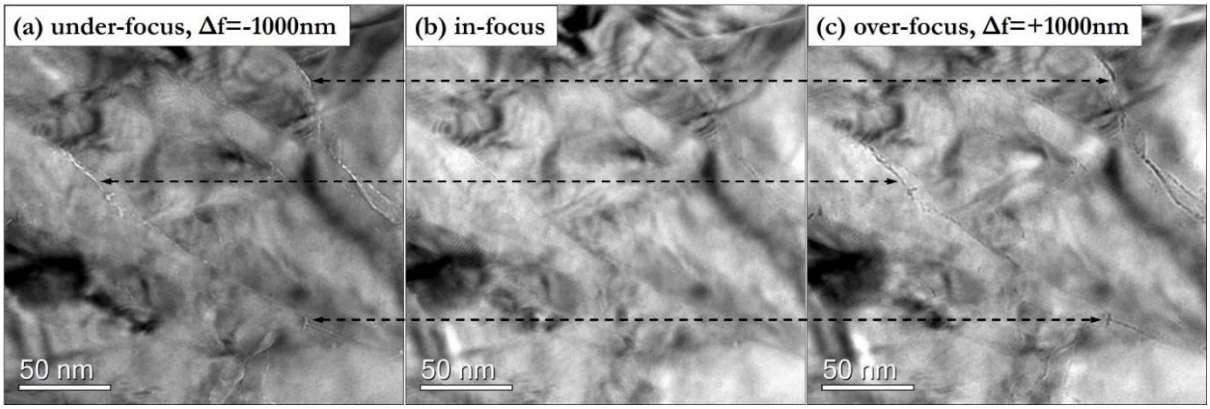

Figure 5: An example of the morphology of nano-pores at grain boundaries in the oxide layer on the Zr-0.5Nb alloy revealed under Fresnel imaging conditions. The dashed arrows identify the same features in the under- and over-focused images

In order to determine the distribution of pores as a function of depth through an oxide layer, a series of Fresnel images must be captured with fixed defocus values (here we have used Δf = ±1000 nm) at various distances from the oxide/metal (O/M) interface. The density (nm. nm^{-3}) of nano-pores measured is then defined as the total length of pores along the oxide growth direction in the region of imaging, and will obviously depend the sample thickness so precise local thickness measurements are required. The thicknesses of the regions of interest in the samples studied were determined using Electron Energy Loss Spectroscopy (EELS) in a JEOL ARM 200F microscope operating at 200kV with a step size of 10nm, a convergence angle of 30mrad and a collection angle of 40mrad. The average thicknesses were determined to be 45nm and 30nm for the oxides on the 75 day and 165 day specimens on the Zr-0.5Nb alloy, respectively

3.2. Results on oxide nano-porosity quantification

The two different samples of the Zr-0.5Nb alloy selected, 75 days and 165 days of exposure had, according to Figure 4 (a) and the C4 model results, drastically different energies for proton migration through the oxide. Areas of approximately the same distance from the oxide/metal interface were chosen for analysis in the TEM specimens as shown in Figure 6 for the 75 days sample. The surface area of each analyzed box is approximately 0.2 – 0.5 μm^2. Two different paths through the oxide were selected (areas 1, 2 and 3 and 4, 5 and 6) in each case to increase the statistical significance of the results since the oxide microstructure can vary extensively over short lateral distances.

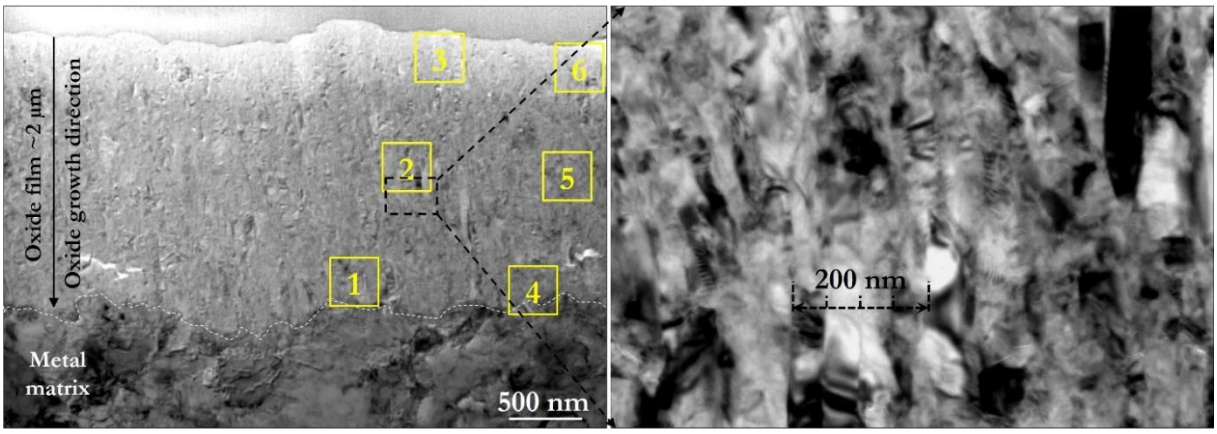

Figure 6: Low magnification TEM image of the whole oxide layer on the Zr-0.5Nb alloy after 75 days exposure. As expected from the weight gain measurements, the oxide thickness is about 2 µm, and the characteristic fine grained columnar microstructure can be seen in the high magnification image on the right. Quantitative porosity analysis has been carried out in the 6 areas marked by yellow squares. The TEM sample thickness in the oxide layer was measured by EELS to be approximately 45nm.

Each of the areas of the kind highlighted in Figure 6 has been carefully analyzed using Fresnel imaging to locate individual pores (as small as 1nm). As an example, intergranular porosity between the columnar ZrO_2 grains lying along the oxide growth direction is clearly observed in Figure 7, but the number and distribution of these pores can also be seen to be markedly different in different regions of the oxide. Qualitatively, interconnected porosity is observed from the oxide/water interface all the way through the oxide layer to about 200nm from the oxide/metal interface. We have chosen to apply the term “non-protective oxide” to define this outer volume of the oxide layer containing this interconnected porosity. Closer to the oxide/metal interface, most of the pores are isolated and offer no short circuit path through the oxide. Although this kind of porosity has been identified previously in similar samples [56], this is the first time that an attempt has been made to measure this porosity quantitatively. This is only possible because the sample thickness is close to the width of individual oxide grains. When the Fresnel images are analyzed using ImageJ® we can extract the density of nanopores at different regions of each oxide, and the results are plotted in Figure 8. The error bars in distance are from measurements of the pore density averaged over the areas studied, while the density error bars are from the variations in pore numbers identified, for instance, in data sets like those from areas 1, 2 and 3 and 4, 5 and 6 identified in Figure 6. Finally, Figure 9 shows a typical over-focused Fresnel image of the oxide on the Zr-1.0Nb (720 °C) alloy exposed for 91 days. In this oxide we observe continuous interconnected porosity at many of the grain boundaries as shown in the circled areas, and

this porosity is observed throughout the oxide thickness. However, no quantitative pore volume density data was acquired for this sample.

4. Discussion

The key observations from Figure 8 are first that there is a clear gradient of pore density across the oxides formed on the Zr-0.5%Nb alloy, with at least 3 times more porosity identified near the oxide/water interface than at the oxide/metal interface. As highlighted earlier, there is also a transition of pore shape from interconnected through most of the oxide layer to mostly isolated pores close to the oxide/metal interface [16, 56]. Secondly, a denser distribution of pores (by a factor of at least 2) is identified close to the oxide/metal interface for the 165 day sample than observed in the 75 day sample. This is direct evidence for an increase of porosity along the ZrO_2 grain boundaries as the oxide thickens. However, this increase in porosity is *not* obviously related to an increase in corrosion rate, since as observed in Figure 3(a), there is no acceleration in corrosion rate of the Zr-0.5%Nb alloy at 165 days. We thus conclude that this nanoscale interconnected porosity is not an effective pathway for the rapid transport of oxygen anions.

On the other hand, the *total* hydrogen pickup fraction varies from 1.4% at 75 days (i.e. the oxide is mostly impervious to hydrogen uptake) to approximately 5% at 165 days. Although this increase in total hydrogen pickup fraction is not large, the *instantaneous* hydrogen pickup fraction, defined as the hydrogen pickup fraction between individual measurements [4] varies significantly between these two time periods. Indeed, the *instantaneous* hydrogen pickup fraction is equal to 4.6% (resp. 1.4%) between 60 and 75 days (resp. 0 and 75 days) of exposure compared to as high as 51.4% (resp. 18%) between 150 and 165 days (resp. 75 and 165 days). Thus the pickup fraction increases by a factor of 12, while the pore density at the oxide/metal interface region increases by a factor of 2, as detailed above, between the two samples. The difference in instantaneous hydrogen pickup fraction is also observed in the C4 model, which predicts a decrease of 0.25eV in the proton migration energy between these two exposure times. Thus there is a clear correlation between the measured increase in hydrogen pickup fraction, the observed increase in interconnected porosity in the oxide and the modelled increase in hydrogen mobility. Of course, in this study, pore density is only characterized across a small area of the entire

oxide and observed trends may not be applicable to the entire oxide, such that more data would need to be collected to validate the above correlation.

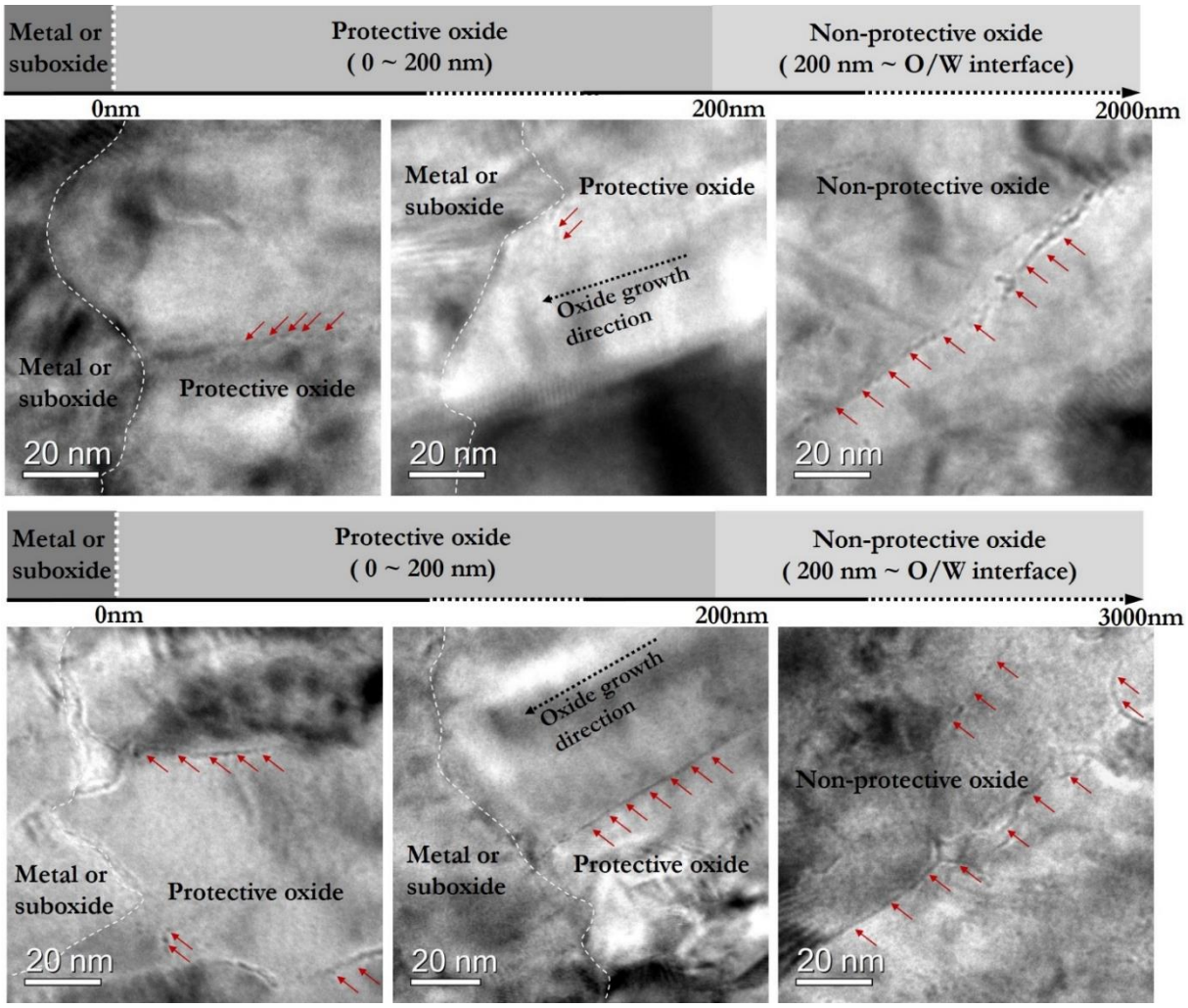

Figure 7: TEM observations of porosity in the oxides formed on the Zr-0.5Nb alloy exposed for 75 days (top) and 165 days (bottom). Nano pores revealed by over-focus Fresnel imaging are marked by red arrows. More interconnected pores are observed in the so-called "non-protective oxide" and isolated pores are observed closer to the oxide/metal interface.

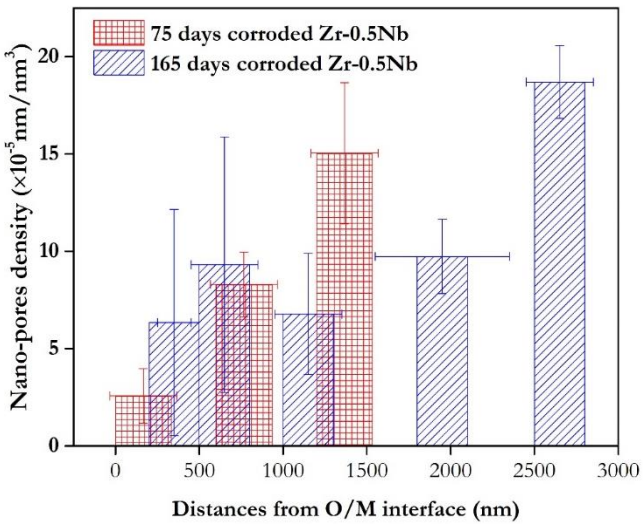

Figure 8: Nano-porosity density as function of the distance from the oxide/metal interface in Zr-0.5Nb samples exposed for 75 days (2.1µm oxide thickness) and 165 days (3.1µm oxide thickness).

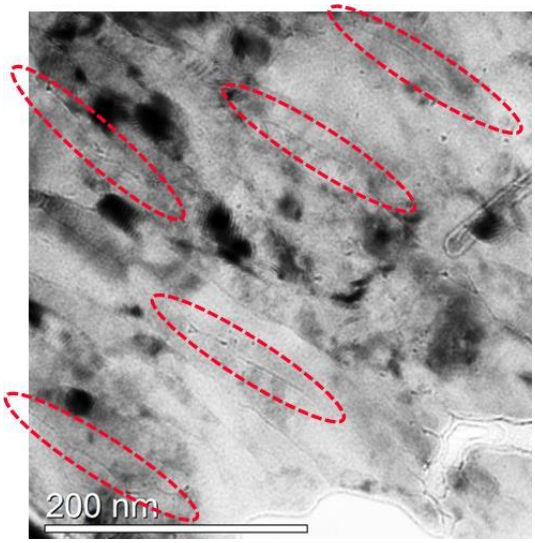

Figure 9: Continuous nano-porosity identified at grain boundaries in an oxide layer formed on the Zr-1.0Nb (720 °C) alloy after exposure for 91 days. This image has been taken a couple hundred micrometers away from the oxide/metal interface and is representative of the inner protective region.

Developing a detailed analysis of the nature of the hydrogenic species and pathways through the oxide is out of the scope of this paper, but some relevant information can be found in the recent literature. For instance, it has been found in [57] that a defect complex consisting of an oxygen vacancy and a hydrogen atom is particularly stable in zirconium oxide; more stable than any other complex defect structure for a wide range of Fermi levels. Although a 1 nm pore is of course very different to an isolated oxygen vacancy, it is possible

that pores are also stable sites for hydrogen atoms and represent preferential migration pathways.

A more detailed ab-initio molecular dynamics study has recently shown that the reaction of water molecules with oxygen vacancies in pores in ZrO_2 plays a key role in the hydrogen pickup mechanism. Indeed, when a water molecule is drawn into such a vacancy site, for instance at the tip of interconnected pores in the non-protective oxide [58], it dissociates to form an acidic (positively charged) and a "hydridic" (negatively charged) hydrogen atom. These hydrogen atoms can recombine forming an H_2 molecule if the reaction takes place in a region where molecular hydrogen can escape into the corroding solution. On the other hand, if H_2 cannot easily escape, as one would expect in the case of deep interconnected nano-porosity, then hydrogen atoms will be more likely to be absorbed in the bulk metal, increasing the hydrogen pickup fraction. Of course the 1D, homogenous, nature of the C4 corrosion model means that it cannot describe that level of microstructural detail; a limitation shared among *all* point defect models published to date. However, the mechanisms detailed above, which are predicted from ab-initio calculations at the nanometer and picosecond scales, could contribute to the decrease of the effective proton migration energy predicted by the C4 model at the micrometer and thousands of hours' scales. It is also important to note that the mechanism proposed in [58] implies that the water can penetrate deep in the oxide via interconnected porosity (called nano-pipes), such that the oxidizing and hydrogen species only diffuse via solid state diffusion across a thin layer of oxide next to the oxide/metal interface. This is different from the present model, which assumes that the oxide is totally impervious to water, such that water reduction occurs at the outer oxide surface. Although there are no clear evidences supporting one or the other hypothesis, the mechanism detailed in [58] should lead to an increase in the oxidation rate as water molecules are being reduced deeper in the oxide (i.e. the migration distance of oxidizing species is shorter as exposure time increases). Since this is not observed experimentally in the oxide protective regime, it could be more appropriate to consider the oxide as impervious to water.

Efficient mesoscale corrosion models are needed to bridge the gap between these different scales. The phase field method has been applied to model oxidation for various materials [59, 60], including zirconium [61, 62], but these zirconium oxidation models did not

account for the impact of oxide electronic conductivity nor for the presence of either grain boundaries or metallic precipitates, so a unified multiscale corrosion model for zirconium alloys is still lacking. Until then, one has to rely on correlations between simplified models and experimental data such as the one highlighted in this study.

5. Conclusions

This study reports an integrated modelling and experimental approach to understand the evolution of the hydrogen pickup fraction observed experimentally in zirconium alloys in service in pressurized water reactors. The main conclusions are:

- The oxidation and hydriding kinetics of two selected ZrNb alloys have been successfully modeled using the C4 model framework. This is the first time that both the oxidation and hydriding kinetics have been modeled using a coupled approach.
- An important outcome of this study is that in order to correctly reproduce the measured oxidation and hydriding kinetics for both alloys, the proton migration energy has to decrease as the transition in oxidation kinetics is approached. For the faster oxidizing Zr-1.0Nb (720 °C) alloy this behavior is repeated throughout the corrosion process, following the periodic transitions in oxide growth rate.
- Using TEM Fresnel imaging, the density of nano-porosity in the oxide corrosion layers has been successfully quantified for the first time as function of both position in the oxide and exposure time.
- A correlation has been found between the relative increase in pore volume density at the oxide/metal interface, as the oxide grows, and the decrease in the effective proton migration energy, as the oxide grows, modeled using the C4 framework. This implies that the presence of pores in the oxide would facilitate the transport of protons to the oxide/metal interface.
- Simple hypotheses have been highlighted to tentatively explain this correlation, but the need for a more complete mesoscale corrosion model bridging temporal and length scales has been stressed.

Acknowledgements

This research was supported by the Consortium for Advanced Simulation of Light Water Reactors (CASL), an Energy Innovation Hub for Modeling and Simulation of Nuclear Reactors

under US Department of Energy Contract No. DE-AC05-00OR22725. The author would like to thank the entire MUZIC community for insightful discussions and guidance over the years.

References

[1] A.T. Motta, A. Couet, R.J. Comstock, Corrosion of Zirconium Alloys Used for Nuclear Fuel Cladding, Annual Review of Materials Research, 45 (2015) 311-343.
[2] M.C. Billone, T.A. Burtseva, R.E. Einziger, Ductile-to-brittle transition temperature for high-burnup cladding alloys exposed to simulated drying-storage conditions, Journal of Nuclear Materials, 433 (2013) 431-448.
[3] X. Wang, M.-J. Zheng, I. Szlufarska, D. Morgan, Continuum model for hydrogen pickup in zirconium alloys of LWR fuel cladding, Journal of Applied Physics, 121 (2017) 135101.
[4] A. Couet, A.T. Motta, R.J. Comstock, Hydrogen Pickup Measurements in Zirconium Alloys: Relation to Oxidation Kinetics, Journal of Nuclear Materials, 451 (2014) 1-13.
[5] J. Romero, J. Partezana, R.J. Comstock, L. Hallstadius, A.T. Motta, A. Couet, Evolution of Hydrogen Pickup Fraction with Oxidation Rate on Zirconium Alloys, in: Top Fuel Reactor Fuel Performance, Zurich, Switzerland, 2015, pp. 476-482.
[6] S. Kass, Hydrogen Pickup in Various Zirconium Alloys during Corrosion Exposure in High-Temperature Water and Steam, Journal of The Electrochemical Society, 107 (1960) 594-597.
[7] M. Harada, R. Wakamatsu, The Effect of Hydrogen on the Transition Behavior of the Corrosion Rate of Zirconium Alloys, in: Zirconium in the Nuclear Industry: 15th International Symposium, ASTM STP 1505, 2008, pp. 384-400.
[8] R. Adamson, F. Garzarolli, B. Cox, A. Strasser, P. Rudling, Corrosion Mechanisms in Zirconium Alloys, in, A.N.T. International, 2007.
[9] A.A. Kiselev, Research on the Corrosion of Zirconium Alloys in Water and Steam at High Temperature and Pressure, in, Atomic Energy of Canada Limited, 1963.
[10] H.G. Kim, S.Y. Park, M.H. Lee, Y.H. Jeong, S.D. Kim, Corrosion and microstructural characteristics of Zr–Nb alloys with different Nb contents, Journal of Nuclear Materials, 373 (2008) 429-432.
[11] H.A. Porte, J.G. Schnizlein, R.C. Vogel, D.F. Fischer, Oxidation of Zirconium and Zirconium Alloys, Journal of The Electrochemical Society, 107 (1960) 506-515.
[12] A.T. Motta, L. Capolungo, L.-Q. Chen, M.N. Cinbiz, M.R. Daymond, D.A. Koss, E. Lacroix, G. Pastore, P.-C.A. Simon, M.R. Tonks, B.D. Wirth, M.A. Zikry, Hydrogen in zirconium alloys: A review, Journal of Nuclear Materials, 518 (2019) 440-460.
[13] I. Charit, K.L. Murty, Creep behavior of niobium-modified zirconium alloys, Journal of Nuclear Materials, 374 (2008) 354-363.
[14] https://www.researchgate.net/project/MUZIC-Mechanistic-Understanding-of-Zirconium-Corrosion-and-Hydrogen-Pick-up, in.
[15] Z. Yu, A. Couet, M. Bachhav, Irradiation-Induced Nb redistribution of ZrNb alloy: an APT study, Journal of Nuclear Materials, In press (2019).
[16] J. Hu, B. Setiadinata, T. Aarholt, A. Garner, A. Vilalta-Clemente, J.M. Partezana, P. Frankel, P. Bagot, S. Lozano-Perez, A. Wilkinson, M. Preuss, M. Moody, C. Grovenor, Understanding corrosion and hydrogen pickup of zirconium fuel cladding alloys: The role of oxide microstructure, porosity, suboxides, and second-phase particles, in: 18th International Symposium on Zirconium in the Nuclear Industry, May 15, 2016 - May 19, 2016, ASTM International, Hilton Head, SC, United states, 2018, pp. 93-126.
[17] B. Setiadinata, Corrosion and Hydrogen Pickup Mechanisms of Zirconium Alloys, in: Department of Materials, University of Oxford, 2016.
[18] A. Couet, A.T. Motta, R.J. Comstock, R.L. Paul, Cold neutron prompt gamma activation analysis, a non-destructive technique for hydrogen level assessment in zirconium alloys, Journal of Nuclear Materials, 425 (2012) 211-217.

[19] B. Cox, Some thoughts on the mechanisms of in-reactor corrosion of zirconium alloys, Journal of Nuclear Materials, 336 (2005) 331-368.
[20] A. Couet, A.T. Motta, A. Ambard, The coupled current charge compensation model for zirconium alloy fuel cladding oxidation: I. Parabolic oxidation of zirconium alloys, Corrosion Science, 100 (2015) 73-84.
[21] A.T. Fromhold, Parabolic Oxidation Of Metals In Homogeneous Electric-Fields, Journal of Physics and Chemistry of Solids, 33 (1972) 95-120.
[22] Y.H. Jeong, H.G. Kim, D.J. Kim, B.K. Choi, J.H. Kim, Influence of Nb concentration in the α-matrix on the corrosion behavior of Zr–xNb binary alloys, Journal of Nuclear Materials, 323 (2003) 72-80.
[23] M. Moorehead, C. A., Z. Cai, J. Hu, Progressing Zirconium-Alloy Corrosion Models Under Irradiation Using Synchrotron XANES, in: 18th International Conference on Environmental Degradation of Materials in Nuclear Power Systems, Portland, OR, 2017.
[24] D.D. Macdonald, The Point Defect Model for the Passive State, Journal of The Electrochemical Society, 139 (1992) 3434-3449.
[25] A. Seyeux, V. Maurice, P. Marcus, Oxide Film Growth Kinetics on Metals and Alloys I. Physical Model, Journal of The Electrochemical Society, 160 (2013) C189-C196.
[26] A. Couet, A.T. Motta, R.J. Comstock, A. Ambard, Hydrogen pick-up mechanism in zirconium alloys, ASTM STP: Selected Technical Papers, (2016).
[27] A. Couet, A.T. Motta, B. de Gabory, Z. Cai, Microbeam X-ray Absorption Near-Edge Spectroscopy study of the oxidation of Fe and Nb in zirconium alloy oxide layers, Journal of Nuclear Materials, 452 (2014) 614-627.
[28] A. Couet, A.T. Motta, A. Ambard, R.J. Comstock, Hydrogen Zirconium Pickup, in: 18th International Symposium on Zirconium in the Nuclear Industry, Hilton Head Island, SC, 2016, pp. 312-349.
[29] B. de Gabory, Y. Dong, A.T. Motta, E.A. Marquis, EELS and atom probe tomography study of the evolution of the metal/oxide interface during zirconium alloy oxidation, Journal of Nuclear Materials, 462 (2015) 304-309.
[30] X. Ma, C. Toffolon-Masclet, T. Guilbert, D. Hamon, J.C. Brachet, Oxidation kinetics and oxygen diffusion in low-tin Zircaloy-4 up to 1523 K, Journal of Nuclear Materials, 377 (2008) 359-369.
[31] M.-H. Chen, B. Puchala, A. Van der Ven, High-temperature stability of δ'-ZrO, Calphad, 51 (2015) 292-298.
[32] B. Puchala, A. Van der Ven, Thermodynamics of the Zr-O system from first-principles calculations, Physical Review B, 88 (2013) 094108.
[33] G.A. Eloff, C.J. Greyling, P.E. Viljoen, The role of space charge in the oxidation of Zircaloy-4 between 350 and 450°C in air, Journal of Nuclear Materials, 199 (1993) 285-288.
[34] J. Ai, Y. Chen, M. Urquidi-Macdonald, D.D. Macdonald, Electrochemical Impedance Spectroscopic study of Passive Zirconium, Journal of Nuclear Materials, 379 (2008) 162-168.
[35] IAEA, Waterside Corrosion of Zirconium Alloys in Nuclear Power Plants, International Atomic Energy Agency, Vienna, 1998.
[36] J.G. Simmons, Poole-Frenkel Effect and Schottky Effect in Metal-Insulator-Metal Systems, Physical Review, 155 (1967) 657-660.
[37] W.S. Chan, C.K. Loh, Electrical Conduction Of Zirconium Oxide Films, Thin Solid Films, 6 (1970) 91-105.
[38] P. Platt, E. Polatidis, P. Frankel, M. Klaus, M. Gass, R. Howells, M. Preuss, A study into stress relaxation in oxides formed on zirconium alloys, Journal of Nuclear Materials, 456 (2015) 415-425.
[39] H. Swan, M.S. Blackmur, J.M. Hyde, A. Laferrere, S.R. Ortner, P.D. Styman, C. Staines, M. Gass, H. Hulme, A. Cole-Baker, P. Frankel, The measurement of stress and phase fraction distributions in pre and post-transition Zircaloy oxides using nano-beam synchrotron X-ray diffraction, Journal of Nuclear Materials, 479 (2016) 559-575.
[40] J. Robertson, K. Xiong, S.J. Clark, Band gaps and defect levels in functional oxides, Thin Solid Films, 496 (2006) 1-7.

[41] Y. Isobe, M. Fuse, K. Kobayashi, Additive Element Effects on Electronic Conductivity of Zirconium-Oxide Film, Journal of Nuclear Science and Technology, 31 (1994) 546-551.
[42] V. Urbanic, M. Griffiths, Microstructural Aspects of Corrosion and Hydrogen Ingress in Zr-2.5Nb, in: Zirconium in the Nuclear Industry: Twelfth International Symposium, ASTM STP 1354, Annecy, France, 2001, pp. 641-657.
[43] M. Moorehead, Z. Yu, L. Borrel, J. Hu, Z. Cai, A. Couet, Comprehensive Investigation of the Role of Nb on the Oxidation Kinetics of Zr-Nb Alloys, Corrosion Science, Submitted (2019).
[44] M. Youssef, B. Yildiz, Predicting self-diffusion in metal oxides from first principles: The case of oxygen in tetragonal ZrO${}_{2}$, Physical Review B, 89 (2014) 024105.
[45] B. Liu, H. Xiao, Y. Zhang, D.S. Aidhy, W.J. Weber, Investigation of oxygen point defects in cubic ZrO2 by density functional theory, Computational Materials Science, 92 (2014) 22-27.
[46] M. Lindgren, I. Panas, Oxygen Vacancy Formation, Mobility, and Hydrogen Pick-up during Oxidation of Zirconium by Water, Oxid. Met., 87 (2017) 355-365.
[47] A. Eichler, Tetragonal Y-doped zirconia: Structure and ion conductivity, Physical Review B, 64 (2001) 174103.
[48] J. Hu, B. Setiadinata, T. Aarholt, A. Garner, A. Vilalta-Clemente, J. Partezana, P. Frankel, P. Bagot, S. Lozano-Perez, A. Wilkinson, M. Preuss, M. Moody, C. Grovenor, Understanding Corrosion and Hydrogen Pickup of Zirconium Fuel Cladding Alloys: The Role of Oxide Microstructure, Porosity, Suboxides, and Second-Phase Particles, Zirconium in the Nuclear Industry, (2018) 93 - 126.
[49] K.-C. Chen, W.-W. Wu, C.-N. Liao, L.-J. Chen, K.N. Tu, Observation of Atomic Diffusion at Twin-Modified Grain Boundaries in Copper, Science, 321 (2008) 1066.
[50] A. Hermann, H. Wiese, R. Bühner, M. Steinemann, G. Bart, Hydrogen Distribution Between Fuel Cladding Metal and Overlying Corrosion Layers, in: ANS International Topical Meeting on LWR Fuel Performance, IAEA, Park City, 2000, pp. 372–384.
[51] Y. Hatano, R. Hitaka, M. Sugisaki, M. Hayashi, Transport mechanism of hydrogen through oxide film formed on zircaloy-4, Journal of Radioanalytical and Nuclear Chemistry, 239 (1999) 445-448.
[52] N.S. McIntyre, R.D. Davidson, C.G. Weisener, B.D. Warr, M.B. Elmoselhi, SIMS studies of hydrogen diffusion through oxides on Zr□Nb alloy, Surface and Interface Analysis, 17 (1991) 757-763.
[53] D. Khatamian, F.D. Manchester, An ion beam study of hydrogen diffusion in oxides of Zr and Zr-Nb (2.5 wt%): I. Diffusion parameters for dense oxide, Journal of Nuclear Materials, 166 (1989) 300-306.
[54] S. Lozano-Perez, A guide on FIB preparation of samples containing stress corrosion crack tips for TEM and atom-probe analysis, Micron, 39 (2008) 320-328.
[55] J.L. Hutchison, L.A. Bursill, Fresnel fringe contrast of faceted voids within gem-quality diamond, Journal of Microscopy, 131 (1983) 63-66.
[56] N. Ni, S. Lozano-Perez, M.L. Jenkins, C. English, G.D.W. Smith, J.M. Sykes, C.R.M. Grovenor, Porosity in oxides on zirconium fuel cladding alloys, and its importance in controlling oxidation rates, Scripta Materialia, 62 (2010) 564-567.
[57] B. Malki, O. Le Bacq, A. Pasturel, Ab initio study of hydrogen related defect in ZrO_2: Consequences on dry and aqueous oxidation, Journal of Nuclear Materials, 416 (2011) 362-368.
[58] E. Wimmer, Materials Modeling of Hydrogen Pickup in Zirconium Alloys, in, EPRI report, 2018.
[59] T.-L. Cheng, Y.-H. Wen, J.A. Hawk, Diffuse-Interface Modeling and Multiscale-Relay Simulation of Metal Oxidation Kinetics—With Revisit on Wagner's Theory, The Journal of Physical Chemistry C, 118 (2014) 1269-1284.
[60] W. You-Hai, C. Long-Qing, A.H. Jeffrey, Phase-field modeling of corrosion kinetics under dual-oxidants, Modelling and Simulation in Materials Science and Engineering, 20 (2012) 035013.
[61] H. El Kadiri, Z.N. Utegulov, M. Khafizov, M. Asle Zaeem, M. Mamivand, A.L. Oppedal, K. Enakoutsa, M. Cherkaoui, R.H. Graham, A. Arockiasamy, Transformations and cracks in zirconia films leading to breakaway oxidation of Zircaloy, Acta Materialia, 61 (2013) 3923-3935.
[62] M. Asle Zaeem, H. El Kadiri, An elastic phase field model for thermal oxidation of metals: Application to zirconia, Computational Materials Science, 89 (2014) 122-129.

[63] L. Borrel, Modeling Corrosion of Zirconium Alloys Fuel Cladding During LOCA HIgh-Temperature Transients Using BISON, in: Engineering Physics, University of Wisconsin-Madison, Madison, WI, 2018.

Appendix: Statistical analysis of the transition

A Monte Carlo approach has been used to conduct a statistical study of the transition time [63]. The transition can be seen as a stochastic process because even though the transition is modeled as an instantaneous process, in reality it takes some time for the protective oxide layer to become porous. A Gaussian distribution for the oxide thickness at transition is then used to account for this non-instantaneous transition. The simulation is run 1000 times using different transition times sampled from the Gaussian distribution (mean: 3.1 µm; standard deviation: 0.15 µm). The oxide thickness evolution with exposure time plot (see Figure 2) with the 1000 curves is transformed into a heat map displaying the density of curves in Figure A-1.

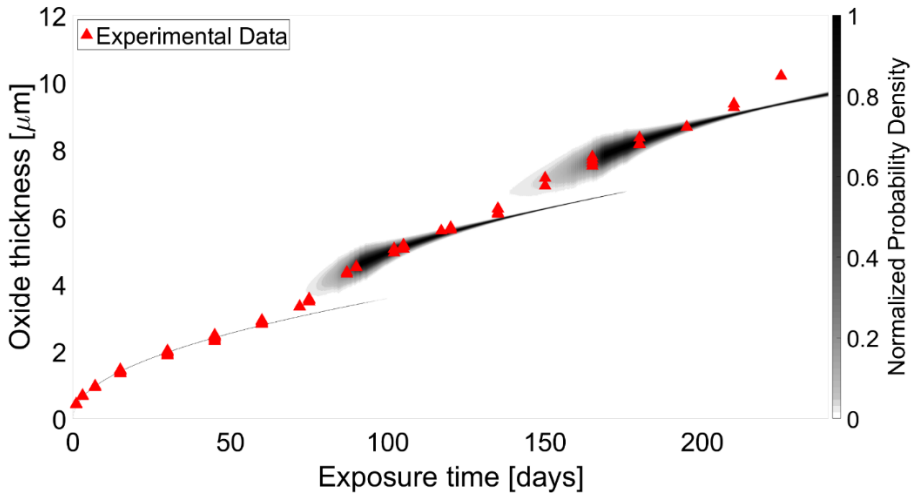

Figure A-1: Oxide thickness versus exposure time heat map; the gray gradient represents the density of curves

The density of curves has been generated by fitting a Gaussian distribution to the oxide thickness distribution at every time step. Special cases are taken for the pre-transition regime (before 75 days) where a Dirac distribution is used, and within the transition region (75-100 days) where a combination of Dirac distribution (for non-transitioned curves) and Gaussian distribution (for transitioned curves) is chosen. The density of curves is then used to generate the 90 % confidence interval displayed in Figure 3.a. The parameters of the Gaussian distribution chosen for the transition oxide thickness (mean: 3.1 µm; standard

deviation: 0.15 μm) have been optimized such that all the experimental data are within the 90 % confidence interval. The standard deviation gives a qualitative estimation of how the transition uncertainty affects the post-transition corrosion kinetics.

Data availability statement:

The raw/processed data required to reproduce these findings cannot be shared at this time as the data also forms part of an ongoing study.